Investigation of the "Block Effect" on Spatial Resolution in PET Detectors

Nada Tomic, *Student Member, IEEE*, Christopher J. Thompson, *Member, IEEE*, and Michael E. Casey, *Member, IEEE*

***Abstract*—Previous studies suggest that when block detectors are used in positron emission tomography (PET) scanners, a "block effect" of about 2 mm should be added in quadrature to the other effects blurring spatial resolution (SR). However, no explanation of the cause of the effect has ever been published. If the effect could be identified, isolated, and reduced then the SR of PET scanners should improve. We studied the origin of the "block effect," using experiments in which all other blurring effects on SR were minimized and precisely determined. Thin, 1 mm wide bismuth germanate (BGO) crystals and a small (1 mm) ^{68}Ge source were used to probe the SR of a HR+ block detector. Two precise translation stages were used to move detectors. We compared coincidence aperture functions (CAFs) for crystals in the block with CAFs of single crystals of various widths. From those measurements, done with one block detector, we concluded that the central crystals in the block showed an additional blurring of 0.8 mm whereas the edge ones showed no additional blurring. When the detectors were separated by 21 cm, the full width at half maximum (FWHM) for central crystals was found to be 2.20 ± 0.04 mm and for edge crystals 1.98 ± 0.04 mm. The FWHM for 4.4 mm width crystals (as used in the HR + block) was estimated to be 2.1 ± 0.2 mm. Results from the crystal identification matrix show that the apparent centroids of the crystals are not located at the geometric centers, which would give errors in the reconstruction algorithm assumed uniform sampling. Our results suggest that the additional blurring previously reported in PET scanners with block detectors is not entirely due to the use of block detectors.**

***Index Terms*—BGO, block detectors, positron emission tomography (PET), spatial resolution.**

I. Introduction

ONE of the major limitations of positron emission tomography (PET) is its spatial resolution (SR). SR in PET depends on positron range, noncolinearity of the annihilation gamma rays, and the width of the detector's crystals. However, when block detectors are used an additional blurring term referred to as the "block effect" has been proposed to account for their poorer SR [1], [2].

In order to reduce the scanner's cost, most modern PET scanners use block detectors in which up to 64 crystal elements are coupled to four photo-multiplier tubes (PMTs). Block detectors use light sharing schemes to identify the crystal that detected annihilation photon. They are much cheaper than detectors with 1:1 coupling between crystals and PMTs. However, there is an uncertainty in the determination of the location of the event within a block detector, due to the presence of multiple crystal elements. In such detectors there appears to be an additional degradation of SR in PET images caused by the use of crystal array. This additional blurring of SR also appears in detectors using many crystals with 1:1 coupling between crystals and photodetectors. Previously, the block effect was reported [1], [2], and SR data were compiled from published reports describing the performance of many PET scanners [2], [3], [17]. Those data suggested that the SR is better in scanners with 1:1 coupling between crystals and PMTs than in those with block detectors. The block effect was reported to be 2.3 mm with the use of light sharing and 1.2 mm without [3], [17]. The fundamental cause of the effect has never been investigated.

There are several possible causes of the "block effect": multiple interactions of the gamma ray within the crystal array, light transport in the scintillation crystal as a function of interaction depth, additional electronic noise due to the use of at least four light sensors, under-sampling of the image with stationary detectors, errors in the crystal identification matrix, and errors due to the effective crystal location being different from its physical location.

One of the possible causes of the additional blurring of SR in block detectors is the existence of multiple interactions of gamma ray within the block This implies that the most of the scintillation light will not originate from the point where the gamma ray first interacts with the detector. In all scintillators, currently used in PET scanners, most 511 keV gamma rays undergo Compton scattering in the crystal before being photo-electrically absorbed. Previously, the mean square distance between the point of the first interaction and the centroid of all the interactions in the crystal was simulated using the Monte Carlo technique. This blurring component was found to be 0.73 mm in bismuth germanate (BGO) detector 30 mm deep and 50 mm wide (as in the ECAT Exact HR+, CTI PET Systems Inc., Knoxville, TN) [4]. This is significantly less than the 2.3 mm reported in actual scanners. In this paper, we report an experimental study of the block detector.

II. Materials and Methods

A. Spatial Resolution of PET Scanners

An empirical formula has been proposed [1], [2] in order to combine the various factors affecting the spatial resolution, which has been written as

$$\mathrm{SR} = 1.25\sqrt{(p_r^2 + \mathrm{ss}^2) + (0.0022 \cdot \mathrm{ds})^2 + (\mathrm{cw}/2)^2 + (\mathrm{be})^2} \quad (1)$$

Manuscript received February 25, 2003. This work was supported by the Natural Science and Engineering Research Council of Canada (NSERC) under Grant 0GP0036672.

N. Tomic is with Department of Radiation Oncology, Jewish General Hospital, McGill University, Montreal, QC H3T 1E2, Canada (e-mail: Nada.Tomic@mail.McGill.Ca).

C. J. Thompson is with the Montreal Neurological Institute and the Medical Physics Department, McGill University, Montreal, QC, Canada (e-mail: Christopher.Thompson@McGill.Ca).

M. E. Casey is with the CTI PET Systems, Inc., Knoxville, TN 37932 USA (e-mail Mike.Casey@CTI-PET.Com).

Digital Object Identifier 10.1109/TNS.2005.851433

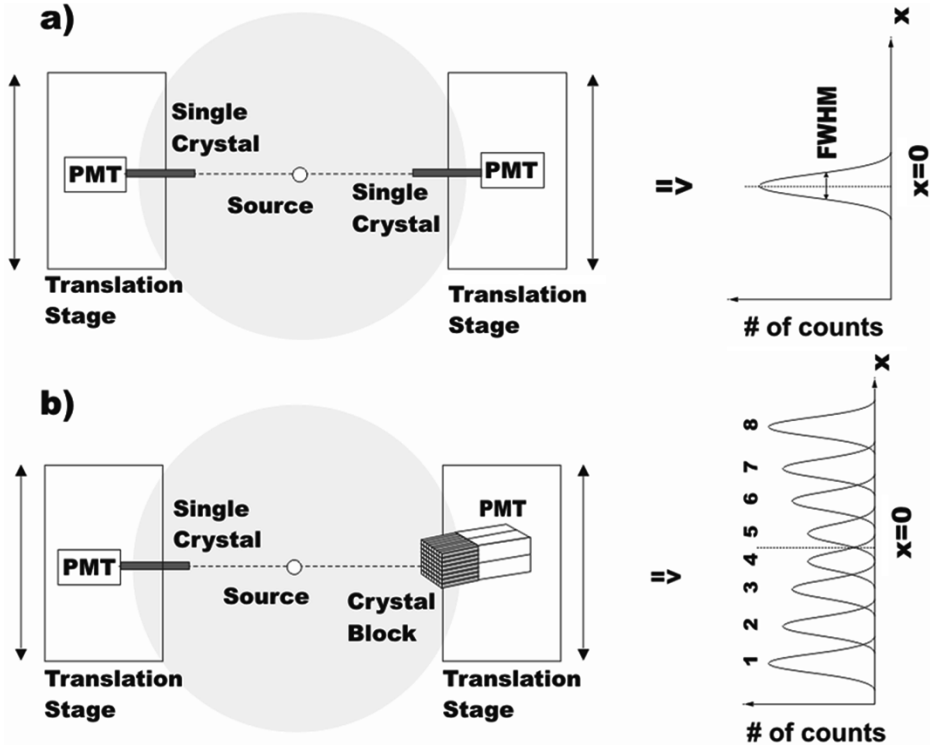

Fig. 1. Set-up for measuring the block effect in CTI HR+ block detector by measuring CAFs when: (a) two single crystals are in coincidence and (b) crystals in the block are in coincidence with single crystals.

where p_r is the mean positron range blurring in image caused by the finite range of the positrons before annihilation, ss is the blurring caused by finite source size, $0.0022 = 1/2 \cdot \tan(0.5°/2)$ is due to the 0.5° mean noncolinearity of the annihilation gamma rays, ds is the detector separation, cw is the blurring introduced by the crystal width, be is the additional blurring due to the use of block detector, and 1.25 is factor that describes the degradation of SR due to the image reconstruction. All the quantities in (1) are given in millimeters. The factor 1.25 may vary according to the reconstruction technique used, and it is likely that most of the scanners which were considered in arriving at this empirical formula (in 1993) used the filtered back-projection technique.

The data from published reports describing SR of several PET scanners are presented by Derenzo *et al.* [2] with the graph of SR as linear function of the crystal width (cw), which is obtained by subtracting the noncolinearity and source size effect on SR. By plotting the SR as a function of cw using (1), including all the blurring effects rather than correcting for them as has been done by others [2], [3], [17], the best possible SR (in the limit of zero width crystals) for any scanner size is more evident. The graph is made assuming 2 mm block effect and no block effect. The different detector separations (ds) correspond to PET scanners used in: human brain imaging (High Resolution Research Tomograph (HRRT) PET with lutetium oxyorthosilicate (LSO) blocks cut into 8×8 and $2.1 \times 2.1 \times 7.5$ mm crystals optically coupled to four PMTs, $\mathrm{ds} = 470$ mm, $\mathrm{cw} = 2.8$ mm, [5]), whole body PET (HR+ with BGO blocks with 8×8 and $4.1 \times 4.4 \times 30$ mm crystals optically coupled to four PMTs, $\mathrm{ds} = 825$ mm, $\mathrm{cw} = 4.4$ mm, [6]), small animal imaging (microPET R4, Concorde Microsystems, Inc. with LSO blocks cut into 8×8 crystals $2.1 \times 2.1 \times 10$ mm optically coupled to a position sensitive (PS) PMT, $\mathrm{ds} = 148$ mm, $\mathrm{cw} = 2.1$ mm, [7]), and high-resolution human breast imaging (Positron Emission Mammography (PEM) with BGO blocks pixilated into 1.9×1.9 mm on two opposite faces, optically coupled to a PS PMT, $\mathrm{ds} = 80$ mm, $\mathrm{cw} = 2$ mm, [8]). All presented SRs from different scanners were measured with 1 mm source size. The measured SRs for those scanners were compared with the obtained theoretical curves. By taking the square root of the differences between squares of the measured and calculated SR, we found the block effect for corresponding scanners and compared it with our result.

B. Experimental Apparatus and Determination of the Effective Source Size

To investigate the block effect we performed experiments in which two detectors in time coincidence record gamma rays from a positron-emitting source. We designed an experimental set-up to measure the coincidence aperture function (CAF) of two single crystals [Fig. 1(a)] and the CAF of the block and single crystal detector [Fig. 1(b)]. The detectors were moved in a direction orthogonal to the collimated gamma-ray beam line with a precision of 0.5 μm. The detectors were mounted on translation stages (Compumotor model 57 102) controlled from an Alpha $4/100$ workstation. Either both detectors were moved in tandem or one of them was at fixed position while the other was moved, depending of the type of the performed measurement. In all experiments, in order to provide appropriate lead shielding, the source remained stationary.

We used a ^{68}Ge "Micro-PET" transmission source, with the activity of 1.4 mCi, sealed in a stainless steel, as a source

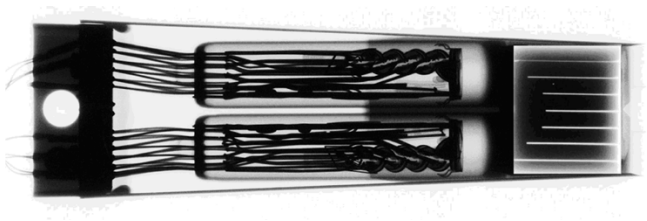

Fig. 2. X-ray image of the CTI HR+ block detector used in these studies.

of 511 keV annihilation photons, which was purchased from Sanders Medical Products Inc. Two thin, 1 mm × 30 mm × 20 mm BGO crystals were purchased from Alpha Spectra Inc. The single crystals, PMTs and charge-integrating amplifiers are enclosed in light-tight aluminum boxes.

The block detector investigated in this work is of the type used in HR+ scanner, and it was provided by CTI. A set of four charge-integrating amplifiers and a high-voltage decoupling network was assembled in a small plastic box. This box and the block detector were attached together to the translation stage. The signals from the four PMTs on the HR+ detector are sent to the summing amplifier. The sum of these signals and the energy signal from the single PMT are acquired with a Jorway Aurora-12 bit analog to digital converter (ADC) CAMAC module and saved in a list file. The ADC is strobed each time a coincidence between the two detectors is identified.

In order to locate the crystals within the block, the HR+ detector was X-rayed at 81 kV, 32 mAs at a distance of 200 cm to visualize the BGO crystal and saw cuts. To show the metal housing of the module and the PMTs we made a second radiograph using 50 kV, 10 mAs, and source to film distance of 110 cm. A composite picture was made and glued to the detector to assist in the alignment during the experiments. Composite X-ray radiograph of the HR+ detector is shown in Fig. 2. The saw cuts are clearly visible and the crystal widths are 4.4 mm for central crystals and 4.2 mm for the edge crystals.

Acquisition software allows the detectors to be pre-positioned and then to move either one or both detectors to the next point without operator intervention. It also allows the spectrum, raw events (in list mode) and images to be saved. During the study, for each source position, an image is created by incrementing a location determined by Anger logic in a 256×256 matrix for each event within a preset energy window. A summed image is also created. The appearance of the summed image is similar to that acquired by block detector exposed to a point source.

The display software has several windows in which the images are analyzed. The main window shows up to 64 images, which are minified to 64×64 matrices. Any image can be zoomed to its full size, and profiles drawn through the crystal territory matrix. Another window allows for placement of up to eight regions of interest (ROI). The count rate in these ROIs can be displayed as a function of the detector positions during the experiment. These graphs correspond to the intercrystal aperture functions. They can be fitted to the sum of three Gaussian functions and the centroid, full width at half maximum (FWHM) and full width at tenth maximum (FWTM) are printed.

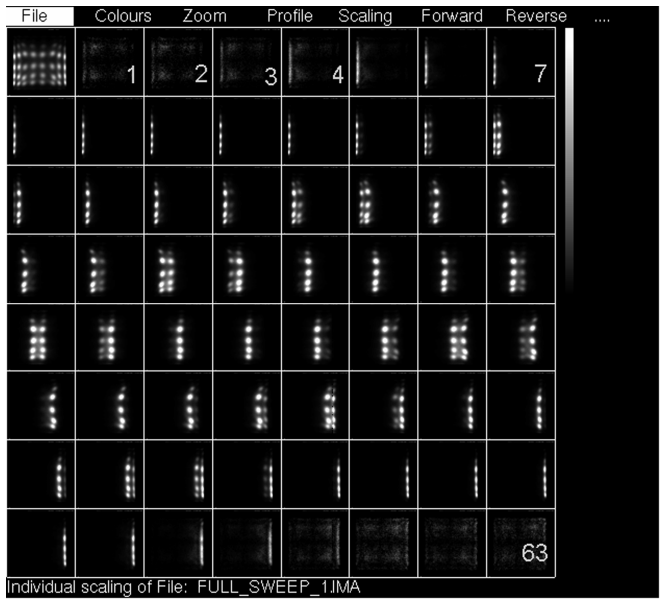

Fig. 3. Data display in the experiments in which crystals in the block detector are in coincidence with 1 mm single crystal. The individual frames present the columns of the crystals in the block that were in coincidence with a single crystal. The picture in the left top corner represents the sum of all individual frames.

Fig. 3 illustrates how the data were displayed in the experiments in which we measured CAFs of different crystals in coincidence. For each set of experiments, 63 individual frames were acquired showing the column of the crystals in the block that were in coincidence with a single crystal. The order of them is shown in Fig. 3 going from left to right and from top to bottom, as the block detector was moving in certain steps while single crystal and the source were fixed positioned. Frames are scaled to their maximum, independently. The first picture, in the top left corner, represents the sum of all the individual frames.

In order to quantify SR measurements we estimated the size of the ^{68}Ge source. We measured CAFs of two 1 mm width BGO crystals at different detector separations. The single crystal detectors were advanced by 0.2 mm between each of 60 acquisitions of 2400 seconds each. The CAF's curves were fitted with three Gaussian functions and the FWHMs for each CAF were calculated. We plotted the square of SR against the square of ds in order to linearize (1), to investigate how the SR behaves with the ds and to estimate the source size. Also, we did the error analysis by taking the errors in estimating FWHM in the three Gaussian fitting of the obtained CAFs.

By taking the square of (1), and neglecting the block effect and image reconstruction effect we obtained

$$\mathrm{FWHM}^2 = (0.0022)^2 \cdot \mathrm{ds}^2 + \left(p_r^2 + \mathrm{ss}^2\right) + \left(\frac{\mathrm{cw}}{2}\right)^2. \quad (2)$$

For 1 mm wide crystals, one obtains $(\mathrm{cw}/2)^2 = 0.25\ \mathrm{mm}^2$. The positron range, $p_r = 0.6$ mm, was estimated based on the average energy of positrons (836 keV) emitted during ^{68}Ge decay. A continuous slowing down approximation (CSDA) range of electrons in steel was taken from the NIST website [9] assuming that it does not differ from the positron range.

C. Measurements of CAF of Various Crystals

In order to measure the block effect in the HR+ block detector we used the same experimental set-up as in Section II-B. On one translation stage, we kept 1 mm wide single crystal. On the other one, we mounted single crystal detectors with various crystal widths. To investigate how the FWHMs of corresponding CAFs behave with changing the cw of the crystals in coincidence, we performed three sets of measurements. The 1.0 mm wide single crystal on the first translation stage was set in coincidence with single crystals 1.0 mm, 3.4 mm, and 7 mm wide positioned on the second translation stage. The detector separation was 21 cm. We collected the counts at 60 different crystal positions in steps of 0.2 mm with acquisition time of 60 seconds. The square of FWHM of the measured CAFs was plotted against the square of the crystal widths. We did the error analysis by taking the errors in estimating FWHM in the three Gaussian fitting of the obtained CAFs. Also, we estimated from the linear fit the value of FWHM for $\mathrm{cw} = 4.4$ mm as it is in an HR+ detector. The error of the FWHM was obtained from the linear fit calculating standard deviation.

We repeated the study with block detector crystals. This experiment was performed for 36 central crystals (whose cw is 4.4 mm), and 12 edge crystals within the block detector (whose cw is 4.2 mm) set in coincidence with the single crystal. The separation between single crystal and the block detector was 21 cm. We collected the counts at 60 different crystal positions in steps of 0.2 mm with an acquisition time of 240 seconds. We measured CAFs for crystals in the block and obtained CAF value distribution among different crystals in the block. We presented FWHM values for crystals in six rows of the block. The first and the last row are missing because of the limitations of the experimental set-up.

The mean values of squares of FWHMs of the measured CAFs for one block detector in coincidence with single crystals were calculated for each column and mean values for central and for edge crystals were determined. We did the error analysis calculating standard deviations for the obtained mean values. In order to estimate the FWHMs of crystals when two block detectors are in coincidence the obtained mean values were multiplied by $\sqrt{2}$.

D. Measurements of Intercrystal Distance in the Block

Previous studies reported that the centroids of interactions in the crystal do not correspond to the geometrical centers of the crystals [10]. In order to determine the separation between the crystals in the HR+ block detector and to assign territory in the crystal identification matrix to appropriate crystals, we performed the following experiment. The crystals in the block were in coincidence with a 1 mm thick crystal. The block detector moved in steps of 0.75 mm while the source and the single crystal detector were at fixed position. We collected data for 2000 seconds. For each set of experiments, 63 frames were acquired. A ROI was placed over each crystal's representation in one row of the obtained crystal identification matrix and counts per minute per pixel (CPM/pixel) were determined for each crystal in each of the 63 frames. In such a way, we obtained eight curves for each crystal in one row. Then, the separations between the peaks of the obtained curves (of the neighboring crystals) were determined. The ROI was also placed over the territory between two crystals and the counts from these regions were plotted as a function of detector position.

In a given direction along the crystal block, there is a probability that the photon is detected in a crystal $i-1$ or in a crystal $i+1$, even if its first interaction was in crystal i. To estimate the fraction of mispositioned events in the crystals, we took a profile along the central row crystals in the crystal identification matrix. The profile was fitted with a multi-Gaussian model, having 25 fitting parameters: eight peaks times three Gaussian function parameters (position, width, and amplitude) and a baseline level. First iterations were performed with the Gaussian functions positions and widths fixed, while the amplitudes varied. In the second set of iterations, the widths varied and finally in the last set of iterations, the positions and the baseline varied, altogether with all the other parameters. From eight Gaussian functions, we calculated the fraction of mispositioned events in a given crystal i in the block detector using

$$P_i = \left(\frac{I_{i-1} + I_{i+1}}{I_i}\right)^2 \tag{3}$$

where I_i is the area of the given crystal i, I_{i-1}, and I_{i+1} are the overlapping areas with the neighboring crystals $i-1$ and $i+1$.

III. Results

A. Spatial Resolution of PET Scanners

Fig. 4 represents the SR as a function of cw for different separations between detectors in coincidence that correspond to commercially available PET scanners: HRRT, HR+, microPET, and PEM, using (1) and assuming positron range of 0.6 mm and 1 mm source size. The solid lines represent a set of curves obtained by assuming no block effect and dashed lines assume the block effect of 2 mm.

For HR+ scanner, the measured SR is very close to the theoretical curve assuming block effect of 2 mm. For microPET R4, HRRT, and PEM system the measured points are below predicted curves, which assume a 2 mm block effect but above the curves that assumes no block effect. Using Fig. 4, we calculated block effects for those scanners by taking the square root of the differences between squares of measured and calculated FWHMs. The results show that the block effect for the scanners is: 1.7 mm (HR+), 1.1 mm (HRRT), 1.2 mm (PEM), and 0.8 mm (microPET).

B. Determination of the Effective Source Size

In Fig. 5, the square of the SR against the square of the ds is plotted, as well as the error bars coming from the estimation of the FWHM in three Gaussian fitting of the obtained CAFs. The FWHM points were fitted using linear fit $y = ax + b$, where y corresponds to FWHM^2, x corresponds to ds^2, parameter a corresponds to the slope of the line, and b is the intercept for ds equal to zero. In Fig. 5, the value of the slope is in a good agreement with the predicted value of $(0.0022)^2$, as given in (2), i.e. $\mathrm{a} = 4.4 \times 10^{-6}$ which gives $\mathrm{a}^{1/2} = 2.09 \times 10^{-3}$. This confirms 0.5° noncolinearity of the annihilation gamma rays. The intercept with y axis for the $\mathrm{ds} = 0$ gives

$$p_r^2 + \mathrm{ss}^2 + \left(\frac{\mathrm{cw}}{2}\right)^2 = 1.605. \tag{4}$$

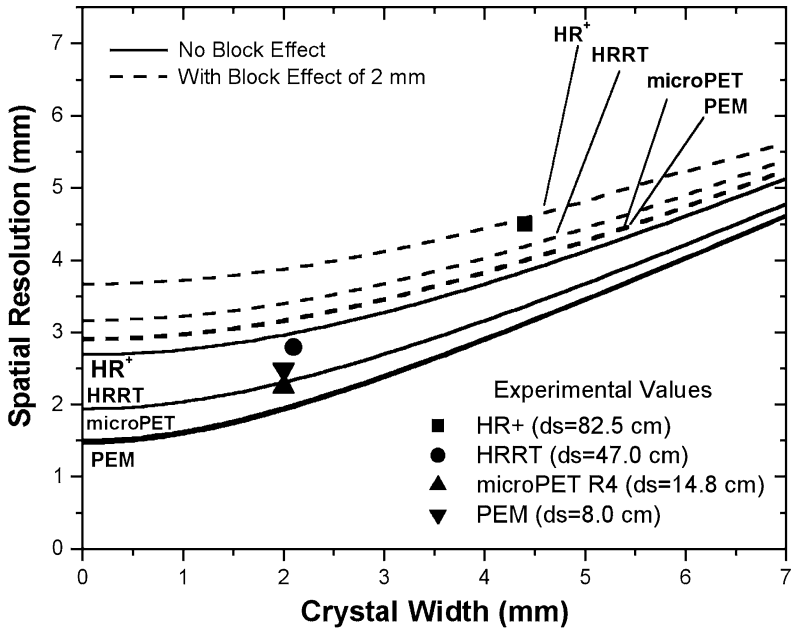

Fig. 4. SR in PET as a function of cw with and without a 2 mm block effect, as obtained from (1). The symbols show the measured SRs for different PET scanners from published reports.

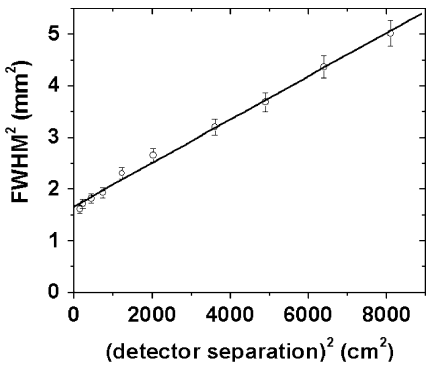

Fig. 5. Variation of the FWHM of CAF of single crystals with detector separation. The error bars represent the errors in calculating the FWHMs using three Gaussian fitting of the obtained CAFs.

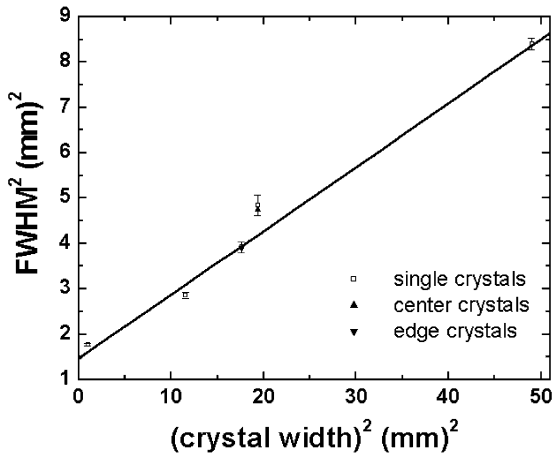

Fig. 6. Variation of the FWHM of CAF of two single crystals (□) with crystal width. The error bars represent the errors in calculating the FWHMs using three Gaussian fitting of the CAFs. Variation of the FWHM of CAF of single crystal with crystals in the block detector (▲, ▼). The error bars represent standard deviations for central and for edge crystals.

The cw in our study is 1 mm, $(\mathrm{cw}/2)^2 = 0.25\ \mathrm{mm}^2$, and the estimated positron range for ^{68}Ge in steel is about 0.6 mm. The linear fit intersects the y-axis for a zero detector separation at an effective source size (the sum of the physical size of the source and the positron range) to be 1.164 mm. We estimated the source size (ss) from the following expression:

$$1.355 = p_r^2 + \mathrm{ss}^2. \tag{5}$$

This gave us the value of 0.99 mm for the source size. This is slightly underestimated because we used CSDA positron range instead of FWHM of the projected path lengths distribution function, which would give us a positron range effect smaller than 0.6 mm.

C. Determination of the CAF of Various Crystals

In Fig. 6, the square of FWHM of the measured CAFs for two single crystals in coincidence is plotted against the square of the various crystal widths, which is presented with circle symbols. The square of the FWHM varies linearly with the square of the cw, in accordance with (1).

We also measured CAFs for crystals in the block and we obtained CAF value distribution among different crystals in the block. In Table I, we presented the corresponding FWHMs for crystals in six rows of the block, as well as mean values and standard deviations for each column.

In Fig. 6, we presented the square of the mean FWHM of the measured CAFs for crystals in the block in coincidence with 1 mm wide single crystal. The results show the mean values: $\mathrm{FWHM\ (for\ central\ crystals)} = 2.20 \pm 0.04$ mm and $\mathrm{FWHM\ (for\ edge\ crystals)} = 1.98 \pm 0.04$ mm. The result for the edge crystals (presented in Fig. 6 with down triangle) coincides with the single crystals fit line whereas the result for central ones (presented in Fig. 6 with up triangle) is above the line. From the linear fit shown in Fig. 6, we obtained: FWHM (for 4.4 mm width crystals, as used in the HR+ block) $= 2.1 \pm 0.1$ mm.

TABLE I
MEASURED CAF VALUE. DISTRIBUTION AMONG DIFFERENT CRYSTALS INSIDE THE BLOCK, SHOWING FWHMS (MM) FOR DIFFERENT CRYSTALS IN THE DETECTOR IN SIX ROWS OF THE BLOCK

Col. row	1	2	3	4	5	6	7	8
2	2.03	2.17	2.22	2.28	2.18	2.22	2.18	1.99
3	1.99	2.20	2.22	2.22	2.18	2.18	2.14	1.99
4	2.06	2.17	2.24	2.24	2.18	2.18	2.13	1.97
5	1.95	2.14	2.19	2.18	2.24	2.22	2.18	1.94
6	1.92	2.14	2.18	2.19	2.18	2.18	2.17	1.99
7	1.95	2.18	2.22	2.22	2.27	2.24	2.20	2.03
mean ± sd	1.98 0.05	2.17 0.02	2.21 0.02	2.22 0.04	2.21 0.04	2.20 0.03	2.17 0.03	1.99 0.03

The edge crystals appear to have similar FWHM as single crystal of the same width. The blurring for central crystals is slightly greater than for single crystals of the same width. From Fig. 6 the discrepancy between squares of measured FWHMs for central crystals and the fitted curve was determined to be 0.63 mm^2. This difference is attributed to the block effect for central crystals in the block having a value of $\mathrm{be} = 0.8$ mm when one block detector is in coincidence with a single crystal. For two block detectors in coincidence we estimated block effect to be $\sqrt{2} \cdot 0.8\,\mathrm{mm} = 1.1$ mm.

D. Measurements of Intercrystal Distance in the Block

Results obtained from the determination of the intercrystal separation in the CTI block detector module are illustrated in Figs. 7 and 8.

In Fig. 7, ROIs were placed over each crystal's representation in a third row, and the CPM/pixel are plotted as a function of distance. The results show that the mean separation of the peaks between central crystals in the block is 4.44 ± 0.13 mm, while on the periphery it is 4.11 ± 0.16 mm. The edge crystals appear to be closer to each other than the central ones. From these results, it appears that crystals in the block do not appear to be uniformly spaced, which confirms the results from the investigation block detector using Anger logic [11].

In Fig. 8, small adjacent regions were placed over the territory spanned by two crystals and the counts from these regions were plotted as a function of distance. Except for two (the lowest intensity) peaks, the peaks are symmetric and their centroids are in identical positions. This suggests that only in a very narrow region approximately midway between the peaks of each crystal's territory, there is a possibility of assigning an event to the wrong crystal. The fraction of mispositioned events in the crystal was calculated using (3) to be 2% for edge crystals up to 4% for central ones, showing that crystals in the block are well separated and that mispositioning of the events in the crystals in the block is small.

IV. DISCUSSION AND CONCLUSION

The various experiments done during this study examined the block effect in the HR+ block detector. The results from our experiment, specifically made to measure the block effect, with all the other factors affecting the SR minimized and precisely determined show that there is additional blurring of 0.8 mm for central and no additional blurring for the edge crystals when one block detector is in coincidence with a single crystal. For two block detectors in coincidence we estimated the block effect to be 1.1 mm. This result suggests that some other effects, apart from block effect alone, could be the reasons of poorer SR in the PET scanners compared by others.

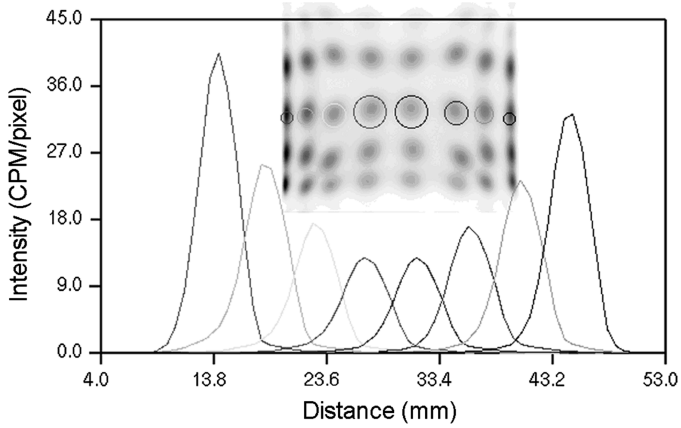

Fig. 7. CPM/pixel as a function of distance for the regions around visible crystals in the image.

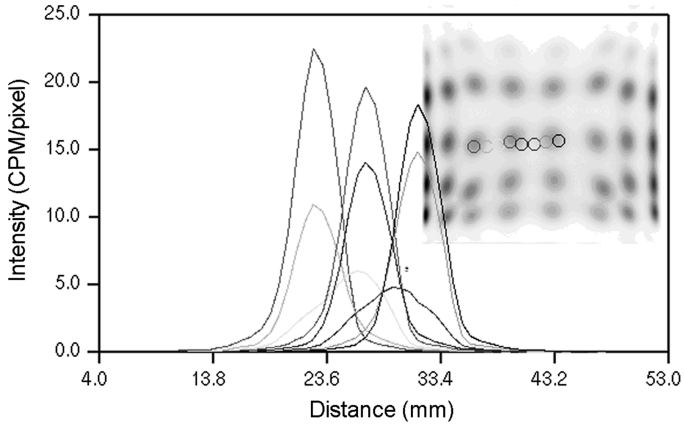

Fig. 8. CPM/pixel as a function of distance for the territories between two crystals in the image.

The Sherbrooke APD scanner [12] is reported to have image SR of 2.1 mm or 2.4 mm, the Donner 600 (Berkeley) scanner [13] 2.6 or 2.9 mm and Tomitani scanner [14] 2.8 mm or 3.5 mm, depending whether the clamshell motion is used or not. The clamshell or wobble motion increases the spatial sampling and improves the SR. Some of the early PET scanners had both high-resolution (wobbled) and low-resolution (stationary) mode scans. The under-sampling, which occurs in the stationary scans, produces poorer SR. Our opinion is that this was not taken into account when SR for different PET scanners were compared with PET scanners with 1:1 coupling between crystals and PMTs [2], [3], [17].

We solved (1) to determine the block effect for the scanners whose spatial resolutions are shown in Fig. 4, we found the block effect to be: 1.1 mm for HRRT, 1.2 mm for PEM-1, and 0.8 mm for microPET R4. All of these are much smaller than previously reported value of 2 mm. The pure block effect might be closer to our experimental result. On the other hand, a total block effect may incorporate other factors that degrade the SR,

which might be dependent on the construction of the detector ring and block detectors within the ring. Evaluation of (1) for the HR+ yields a block effect of 1.7 mm. For the HR+ PET scanner, these effects may have been much more pronounced than in the other three models. We found that the contribution from the central crystals is only 1.1 mm.

From the determination of the separation between crystals in the HR+ block detector and the assignment of territory in the crystal identification matrix to appropriate crystals, we concluded that the crystals do not appear to be uniformly spaced in the block. This must be taken into account when reconstructing images. Also, our results suggest that only in a very narrow region between the peaks of each crystal's territory, there is a possibility of assigning an event to the wrong crystal. The calculated rate of mispositioned events in the crystals shows that crystals in the block are well separated.

Our study suggests that the measured CAFs and nonuniform sampling are not sufficient to explain the 2.3 mm block effect, which has been observed by Lecomte [3], [17], and proposed and observed by Moses [1], [2]. However, when their theoretical equations are plotted as in Fig. 4, the SR of the HR+ scanner is very close to the curve corresponding to a 2 mm block effect. This could be due to under-sampling of the image space with stationary detectors. This present study was aimed at the intrinsic properties of the block effect rather than the effects of under-sampling. Experiments on a complete PET scanner have now been performed. These experiments isolate the under-sampling effects from intrinsic blurring from block detectors. Our preliminary findings were presented at the 2004 meeting of the Society of Nuclear Medicine [15] and a more complete report will appear later [16].

REFERENCES

[1] W. W. Moses and S. E. Derenzo, "Empirical observation for spatial resolution degradation in positron emission tomographs using block detectors," *J. Nucl. Med.*, vol. 33, no. 5, p. 101P, 1993.

[2] S. E. Derenzo, W. W. Moses, R. H. Huesman, and T. F. Budinger, "Critical instrumentation issues for <2 mm resolution, high sensitivity brain PET," in *Quantification of Brain Function*, K. Uemura, N. A. Lassen, T. Jones, and I. Kanno, Eds. Amsterdam, The Netherlands: Elsevier, 1993, pp. 25–37.

[3] R. Lecomte, private communication, 1998 personal communication.

[4] C. J. Thompson, "The effects of detector material and structure on PET spatial resolution and efficency," *IEEE Trans. Nucl. Sci.*, vol. 37, no. 2, pp. 718–724, 1990.

[5] R. Boellaard, F. Buijs, H. W. A. M. de Jong, M. Lenox, T. Gremillion, and A. A. Lammertsma, "Characterization of a single LSO crystal layer high resolution research tomograph," *Phys. Med. Biol.*, vol. 48, pp. 429–448, 2003.

[6] G. Brix, J. Zaers, L. E. Adam, M. E. Bellemann, H. Ostertag, H. Trojan, U. Haberkorn, J. Doll, F. Oberdorfer, and W. J. Lorenz, "Performance evaluation of a whole-body PET scanner using the NEMA protocol," *J. Nucl. Med.*, vol. 38, no. 10, pp. 1614–1623, 1997.

[7] C. Knoess, S. S. Siegel, D. Newport, N. Richerzhagner, A. Winkler, A. Jacobs, R. N. Goble, R. Graf, K. Wienhard, and W. D. Heiss, "Performance evaluation of the microPET R4 PET scanner for rodents," *Eur. J. Nucl. Med. Mol. Imaging*, vol. 30, no. 5, pp. 737–747, 2003.

[8] C. J. Thompson, K. Murthy, Y. Pickard, I. N. Weinberg, and R. Mako, "Positron emission mammography (PEM): A promising technique for detecting breast cancer," *IEEE Trans. Nucl. Sci.*, vol. 42, no. 4, pp. 1012–1017, Aug. 1995.

[9] J. H. Hubbel and S. M. Seltzer. Tables of X-Ray Mass Attenuation Coefficients and Mass Energy-Absorption Coefficients. [Online]. Available: http://www.physics.nist.gov/PhysRefData/XrayMassCoef/cover.htm

[10] Y. Picard and C. J. Thompson, "Determination of the centroid of interaction of the crystals in block detectors for PET," *IEEE Trans. Nucl. Sci.*, vol. 41, no. 4, pp. 1464–1468, Aug. 1994.

[11] M. Dahlbom and E. J. Hoffman, "An evaluation of a two-dimensional array detector for high resolution PET," *IEEE Trans. Med. Imag.*, vol. 7, no. 4, pp. 264–271, Dec. 1988.

[12] R. Lecomte *et al.*, "Initial results from the Sherbrooke avalanche photodiode positron tomograph," *IEEE Trans. Nucl. Sci*, vol. 43, no. 3, pp. 1952–1957, Jun. 1996.

[13] S. E. Derenzo, R. H. Huesman, J. L. Cahoon, A. Geyer, D. Uber, T. Vuletich, and T. F. Budinger, "A positron tomograph with 600 BGO crystals and 2.6 mm resolution," *IEEE Trans. Nucl. Sci.*, vol. 35, no. 1, pp. 659–664, Feb. 1988.

[14] T. Tomitani, N. Nohara, H. Morayama, M. Yamamoto, and E. Tanaka, "Development of a high resolution positron CT for animal studies," *IEEE Trans. Nucl. Sci.*, vol. NS-32, no. 1, pp. 822–825, Feb, 1985.

[15] C. J. Thompson, N. Tomic, M. Hinse, and S. Richard, "Blurring of images from PET scanners due to under-sampling of the image space," *J. Nucl. Med.*, vol. 45, p. 167, 2004.

[16] C. J. Thompson, S. S. James, and N. Tomic, "Under-sampling in PET scanners as a source of image blurring," *Nucl. Instrum. Meth. Phys. Res.* (A), Oct. 2004, submitted for publication.

[17] Based on data presented at the conference on High Resolution Imaging in Small Animals with PET MR and Other Modalities, Amsterdam, The Netherlands, Sep. 1999.